

Modeling the Effect of Periodic Wall Roughness on the Indoor Radio Propagation Channel

Vincent A. Fono* and Larbi Talbi

Abstract—A deterministic model based on ray tracing and dealing with periodic roughness is developed, for an indoor radio propagation channel and experimentally validated at a frequency of 10 GHz. Two different scenarios are studied, namely a smooth corridor and a corridor having artificial periodic roughness. The periodic roughness consists of a set of conductive semi-cylinders attached to the corridor sidewalls. Two different antenna setups are considered during the measurements, horn-horn antennas and patch-patch antennas, in transmitter-receiver configurations. Excellent agreement is achieved in terms of the received powers versus distance and the power delay profiles. The signal fading is analyzed. The statistical parameters are also generated, and a good agreement is observed between the simulation and measurement results.

1. INTRODUCTION

Radio propagation in wave guiding structures such as tunnels, canyons and corridors have received increasing interest from cellular networks operators and the research community. Many of the recent studies have focused on Radio-Local Area Network (R-LAN) and Personal Communication Services (PCS) [1–3]. In these wireless systems, the main concern was the study of the received power in terms of the receiver position [4]. Moreover, indoor propagation exhibits both large scale and small scale multipath fading, which affect the signal quality and limit transmission data rates. Hence, the last generation of communication systems incorporates Multiple Input Multiple Output (MIMO) antenna systems that are known to exploit fading and improve signal transmission quality. The study of multipath fading in MIMO systems starts with an understanding of this phenomenon in the simpler Single Input Single Output (SISO) systems, where deterministic and statistical models are considerably simpler to develop.

Wireless channel models aim to predict the effect of the channel without the expense of deploying a dedicated measurement system. Different modeling techniques exist and differ in terms of accuracy and complexity. The development of a deterministic model requires an understanding of the signal wave propagation behaviour inside confined environments such as buildings. Depending on the walls' surface roughness, radio waves may experience reflection, refraction, diffraction and scattering (from rough surfaces and in-building furniture). Pertaining to straight corridors, several radio wave channel characterization and modeling studies have been published in the last decades [2, 5–9]. For instance, the propagation environment of an open-trench drain was explored for Line-Of-Sight (LOS) and Non-Line-Of-Sight (NLOS) conditions by carrying out field measurements at 900 MHz, 2.4 GHz and 5.8 GHz [2]. Three different polarization arrangements (vertical-vertical, horizontal-vertical and horizontal-horizontal) were taken into account and the path loss exponent of the propagation model was derived. In another study, the performance of an ultra-high frequency Radio Frequency Identification (RFID) system operating at 869 MHz was validated using propagation models and

Received 28 April 2016, Accepted 12 August 2016, Scheduled 25 August 2016

* Corresponding author: Vincent Adelphe Fono (fonv02@uqo.ca).

The authors are with the Department of Computer Science and Engineering, University of Quebec — UQO, Gatineau, Canada.

practical measurements [7]. Moreover, ray-based models in indoor corridors were proposed in [8], and compared with results from vertically and horizontally polarized propagation channel measurements in the 60 GHz frequency band. Additionally, the multipath power richness has been studied extensively, for different environments and frequency bands. Some received signal strength measurements have been reported in [9] as a mean to validate a ray tracing model at 900 and 1800 MHz frequency bands. The study concludes that ray tracing models, neglecting diffraction effects, perform better on LOS scenarios than on NLOS ones.

In a previous work [10], a deterministic model, able to predict radio wave propagation in a rough tunnel with periodical profile, was presented. The model concerned the 60 GHz frequency band and compared the results obtained for smooth walls, such as, path loss (PL), impulse response, and coherence bandwidth with those of rough walls. However, no experimental measurements were performed at that time to validate the model. In this paper, however, the deterministic model presented, based on ray tracing, is experimentally validated in a rough and a smooth corridor at 10 GHz. The received power is predicted through simulation and compared with real measurements. Narrowband and wideband modeling approaches are developed. Moreover, statistical analysis is performed in order to determine the PL exponent and study the fast and slow fading characteristics.

The proposed model may have applications in many factories and sensitive environments where metallic, stainless steel or aluminium cylindrical tanks and tubes are used [11–13]. Such cylinders are most of the time arranged to be bracketed to a wall mounted installations using frame for multiple cylinder free standing installation supplied by the fire extinguishing system's installer [12, 14]. The cylinders can be present in the structure as oil, wine, fuel and gas storage tanks or as fire prevention systems and especially as fixed mounted fire suppression systems. Such systems are essential to protect data centers, control rooms, server rooms, electrical rooms, telephones rooms, archive and storage rooms [11, 12]. These modern fire suppression systems are fully automatic as they don't require a person to hear alarm or take action [12]. Therefore propagation modeling can be helpful for designing fire detection and alarm systems in such corridors or indoor environments. In accordance to the typical assembly of the gas cylinder installation close to the rough area studied in [10], validation of the proposed model could be very helpful to understand the behavior of electromagnetic waves in a real location containing a gas fire suppression system.

To the best of the authors' knowledge, no study of the effect of surface roughness on wave propagation, based on ray tracing and statistical analysis, has been performed at the 10 GHz band. The rest of the paper is organized as follows: In Section 2, a deterministic model that predicts the received power in terms of the transmitter-receiver (Tx-Rx) separation distance is described. In Section 3, narrowband and wideband measurement results are presented to validate the simulation model. In Section 4, large scale and small scale propagation mechanisms are obtained and statistically analyzed. Finally, the paper is concluded in Section 5.

2. PROPOSED MODEL

In this study, a deterministic model based on Geometrical Optics combined with the Uniform Theory of Diffraction (GO-UTD) is developed. The first step consists of a well-known 3-D ray tracing model for empty narrow corridor with smooth wall surfaces [3, 5, 15, 16]. Then, the model is extended to deal with rough wall surfaces by introducing the effect of scattering. Subsequently, the measurement procedure for the model validation is presented.

2.1. Indoor Measurement Scenario and Building Description

Figure 1 shows a photograph of the propagation environment where the artificial roughness is clearly identified. Figure 1(a) represents the smooth corridor and Figure 1(b) denotes the rough corridor made of steel semi-cylinders attached to the corridor with smooth side walls. The environment studied is a straight narrow corridor whose dimensions are 24.6 m long, 1.8 m wide and 2.43 m high. It is located in the second floor of the Lucien-Brault building at the University of Quebec in Outaouais (UQO). The geometry sketch of the rough surface profile is also given with its top and side views in Figure 2.

Figure 2 illustrates the geometry of the rough corridor where $R = 8$ cm and $D = 2R = 16$ cm

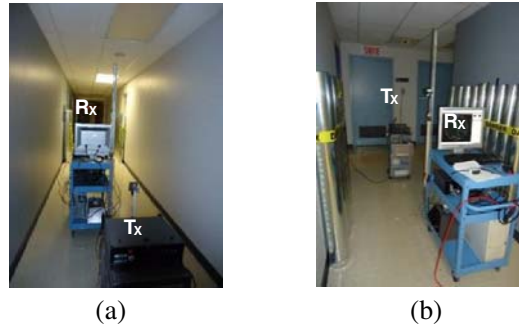


Figure 1. Photography of the undertaken corridor and the measurement setup. (a) Smooth corridor. (b) Rough corridor.

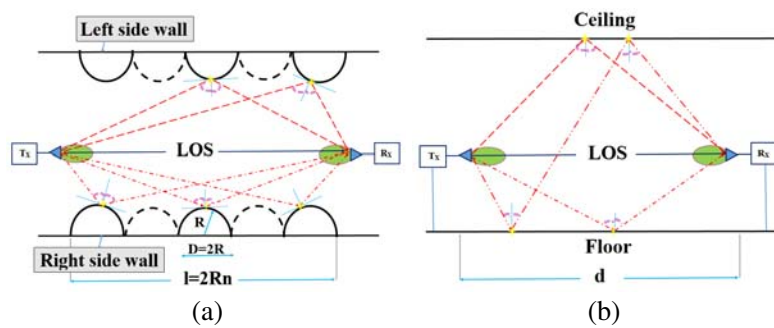


Figure 2. Geometry sketch of the rough corridor profile. (a) Top view. (b) Side view.

Table 1. Dielectric parameters of the corridor materials [17].

Material	Ceiling	Floor	Side Walls	Steel rough profile (Metal)
ϵ_r (F/m)	1.5	5.31	2.94	1
σ (S/m)	0.0131	0.3780	0.1064	10^7
thickness (m)	0.03	0.3	0.003	0.0015

are the radius and diameter of each of the n semi-cylinders respectively, $n = 10$ is the number of semi-cylinders forming the periodic roughness on each of the side walls and $l = 2Rn = 160$ cm represents the total length over which the periodic roughness is distributed.

The electromagnetic properties of the corridor materials are described in Table 1, where ϵ_r and σ are the relative permittivity and the conductivity respectively [17]. The modeling technique is based on these parameters to calculate the scattering (or diffraction from the rough surface) and reflection (on the flat surfaces) coefficients used to get the simulation results.

2.2. Narrowband and Wideband Channel Modeling

The analytical study of the radio wave propagation, in the rough corridor described in Figure 1, is performed in two parts. Firstly, a narrowband model is derived. Then, the channel impulse response for wideband channel is determined. The two modeling techniques allow to predict the electromagnetic wave propagation in the corresponding corridor.

2.2.1. Narrowband Channel Modeling

In order to compute the narrowband parameters of the studied propagation channel, the rough profile is divided into a set of n smooth perfectly conducting convex surfaces. Hence, the undertaken problem consists in a diffraction (or scattering) of an arbitrary electromagnetic ray by a smooth perfectly conducting convex semi-circular surface. Our approach consists in using GO to locate all realistic rays, traveling from the transmitter to the receiver, that satisfy the generalized Fermat's principle [18]. Then, using UTD, the received power, from scattering on the rough profile, is derived by combining the powers from all scattering paths. Moreover, the reflected path powers on both the floor and the ceiling are expressed using ray-tracing [5, 15]. The analytical formula of the proposed propagation model, computing the total received power, is expressed as follows:

$$P_R = \left(\frac{\lambda}{4\pi} \right)^2 P_T \left| \sum_w \sqrt{G_T(\theta_w) G_R(\theta_w)} \cdot u^i(d_w) \cdot \prod_l (\sqrt{\rho_{1l}^r \rho_{2l}^r}) \Gamma_{Fock}(\theta_{lw}) \prod_m R_{Fresnel}(\theta_{mw}) \right|^2 \quad (1)$$

where P_T is the transmitted power; $G_T(\theta_w)$ and $G_R(\theta_w)$ are the radiation patterns of the transmitting and the receiving antennas, respectively; $u^i(d_w)$ is the incident field of the w th ray with an unfold length d_w which is determined using analytical geometry theory and numerical methods, as described in [18]. $\Gamma_{Fock}(\theta_{lw})$ and $R_{Fresnel}(\theta_{mw})$ are the Fock scattering and Fresnel reflection coefficients, respectively. θ_{lw} and θ_{mw} are the reflection angles of a given w th path that intercepted the rough profile by l reflections and the planar sides of the corridor (lateral walls, ceiling or floor) by m reflections. ρ_{1l}^r and ρ_{2l}^r are the principal radii of curvature for the l th location in which the w th path interacts with the rough surface [19].

Figure 3 depicts a detailed geometry for the scattering path that occurs on one of the cylinders forming the rough surface.

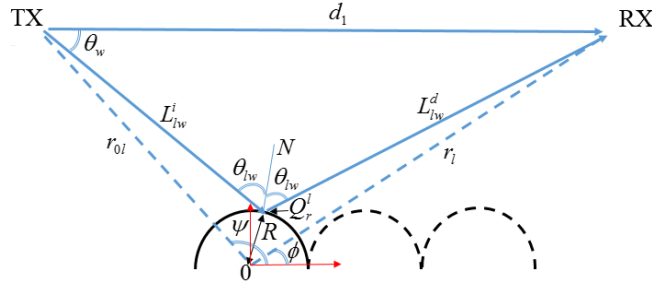


Figure 3. Detailed geometry of scattering problem leading to Eq. (1).

Additional details regarding the computation of $\Gamma_{Fock}(\theta_{lw})$ and $R_{Fresnel}(\theta_{mw})$ are provided in [3, 19, 20].

$\Gamma_{Fock}(\theta_{lw})$ is the Fock reflection coefficient also named the generalized reflection coefficient [18]. It is described by three parameters; the first parameter is the modified Pekeris caret function coefficient (named Fock scattering function) \tilde{p} ; the second parameter is a transition function (named Fresnel integral) F defined as $F(x) = 2j\sqrt{x}e^{jx} \int_{\sqrt{x}}^{+\infty} e^{-jt^2} dt$; the third parameter is the Fock parameter $\xi^r(\theta_{lw}) = -2M \cos \theta_{lw}$ where $M = \left(\frac{kR}{2}\right)^{1/3}$ is the value of curvature parameter at the reflection point on each semi-cylinder; the parameter $X^r(\theta_{lw}) = 2k \frac{L_{lw}^i L_{lw}^r}{L_{lw}^i + L_{lw}^r} \cos^2(\theta_{lw})$ is the Fresnel integral parameter [18]. $k = \frac{2\pi}{\lambda}$ is the wave number.

$$(\Gamma_{Fock}(\theta_{lw}))_e = -\sqrt{-\frac{4}{\xi^r(\theta_{lw})}} e^{-j\left(\frac{\xi^r(\theta_{lw})}{12}\right)} \left\{ \tilde{p}(\xi^r(\theta_{lw})) - \frac{e^{-j\frac{\pi}{4}}}{2\xi^r(\theta_{lw})\sqrt{\pi}} F(X^r(\theta_{lw})) \right\} \quad (2)$$

ρ_{2l}^r is defined by the relationship $\frac{1}{\rho_{2l}^r} = \frac{1}{\rho_{1l}^r} + \frac{2}{R \cos(\theta_{lw})}$, where $\rho_{1l}^r = L_{lw}^i$ and R the radius of curvature of each semi-cylinder. For the reflection on flat surfaces, the Fresnel reflection coefficients are expressed as:

$$R_{Fresnel}(\theta_{mw}) = \begin{cases} \frac{-\varepsilon_r \cos(\theta_{mw}) + \sqrt{\varepsilon_r - \sin^2(\theta_{mw})}}{\varepsilon_r \cos(\theta_{mw}) + \sqrt{\varepsilon_r - \sin^2(\theta_{mw})}} & \text{for } E \text{ polarisation} \\ \frac{\cos(\theta_{mw}) - \sqrt{\varepsilon_r - \sin^2(\theta_{mw})}}{\cos(\theta_{mw}) + \sqrt{\varepsilon_r - \sin^2(\theta_{mw})}} & \text{for } H \text{ polarisation} \end{cases} \quad (3)$$

The point Q_r^l in Figure 3 is determined by solving the following transcendental equation obtained by applying Fermat's principle:

$$g(\theta_{lw}) = \frac{R - r_{0n} \cos(\theta_{lw} - \psi)}{\sqrt{R^2 + r_{0n}^2 - 2Rr_{0n} \cos(\theta_{lw} - \psi)}} - \frac{R - r_n \cos(\theta_{lw} - \phi)}{\sqrt{R^2 + r_n^2 - 2Rr_n \cos(\theta_{lw} - \phi)}} = 0 \quad (4)$$

Then the total path length d_w of diffraction by a semi cylinder is derived as $d_w = L_{lw}^i + L_{lw}^d$. With $L_{lw}^i = \sqrt{R^2 + r_{0n}^2 - 2Rr_{0n} \cos(\theta_{lw} - \psi)}$ and $L_{lw}^d = \sqrt{R^2 + r_n^2 - 2Rr_n \cos(\theta_{lw} - \phi)}$. Next the incident field of the unfolded path d_w is expressed as $u^i(d_w) = \frac{e^{-jk d_w}}{d_w}$.

The propagation path loss (PL) can be derived from (1) as the ratio of P_R/P_T .

2.2.2. Wideband Channel Modeling

The wideband model consists in finding the channel frequency response in the $[f_0 - f_{N-1}]$ frequency band, for a fixed Tx-Rx separation distance d . From (1), the channel frequency response is obtained by combining the attenuation factors of each ray of the model.

The transfer function is denoted by:

$$H(f) = \left(\frac{\lambda}{4\pi}\right) \sum_w \sqrt{G_T(\theta_w) G_R(\theta_w)} \cdot u^i(d_w) \cdot \prod_l (\sqrt{\rho_{1l}^r \rho_{2l}^r}) \Gamma_{Fock}(\theta_{lw}) \prod_m R_{Fresnel}(\theta_{mw}) \quad (5)$$

The channel impulse response is then expressed as:

$$h(t) = \frac{1}{N} \sum_{v=1}^N \sum_w a_{wv} \delta(t - \tau_w) \quad (6)$$

where $a_{wv} = \sqrt{G_T(\theta_w) G_R(\theta_w)} \cdot u^i(d_w) \cdot \prod_l (\sqrt{\rho_{1l}^r \rho_{2l}^r}) \Gamma_{Fock}(\theta_{lw}) \prod_m R_{Fresnel}(\theta_{mw})$ is the frequency-dependent attenuation of w th path in the v th frequency sub-band; $\tau_w = \frac{d_w}{c}$ is the propagation delay associated with the w th path [21].

The RMS delay spread and the coherence bandwidth, which characterize the time and frequency dispersive properties, are expressed as follows:

$$\tau_{\text{RMS}} = \sqrt{\overline{\tau^2} - \bar{\tau}^2} \quad (7)$$

where $\bar{\tau}$ denotes the mean excess delay and $\overline{\tau^2}$ is the second moment of the Power Delay Profile (PDP) [22].

$$B_C = \frac{1}{5\tau_{\text{RMS}}} \quad (8)$$

3. NARROWBAND AND WIDEBAND CHANNEL MEASUREMENTS

In order to validate the proposed models, previously discussed, two different measurement campaigns have been conducted using a VNA (Agilent N5247A vector network analyzer of Keysight Technologies [23]). The experimental validation is done in the X-Band, precisely, at 10 GHz due to the significantly smaller path loss compared to K_a and V bands. Several applications as radio-localisation

can be applied at this band. Moreover, alarm systems are generally designed to operate in this frequency band [24].

The first campaign consists of the continuous wave (CW) measurements taken at 10 GHz with two types of antennas arrangement (patch-patch and horn-horn). For each antennas arrangement, the transmitter (Tx) and the receiver (Rx) are positioned in the middle of the corridor as described in Figure 1. The receiver is mounted on a trolley at a height $h_t = 1.3$ m and is initially positioned at $d_0 = 1$ m from the transmitter. The transmitter and the receiver are positioned at the same height from the floor. In order to measure both the fast and the slow fading, the distance between two consecutive measurement points is set at 0.3λ [25–28].

The second set of measurements is carried out in a wide frequency band, exactly in the X band. The complex channel transfer function is measured in the [8 GHz–12 GHz] frequency band. System calibration is performed with the cables connected to the VNA in order to remove the cable induced phase shifts from the frequency response $H(f) = S_{21}$. Table 2 specifies the different devices used to carry out the measurement campaign.

Figure 4 provides the antennas photography associated to their normalized radiation patterns in E and H planes.

4. RESULTS AND ANALYSIS

4.1. Narrowband Results

The validation of the model is done by comparing experimental and predicted results at the frequency of $f = 10$ GHz. Figure 5 shows the predicted and measured received power levels for the scenario described in Figure 1(b). This scenario takes into account the effect of roughness on the received power when the transmitter is fixed in the middle of the corridor and the receiver is moved at a very slow speed along a straight path away from the transmitter. Simulation results are compared to the recorded CW measurements for both antenna pairs. The maximum number of reflections and scattering, on the semi-circular surface, that a ray can undergo is set to 2. Due to the filtering properties of the antenna beam-width, the realistic rays depend on the type of antennas used in the modeling and the measurements.

Table 2. Measurement parameters.

Parameter	Value
Center frequency	10 GHz
Bandwidth	4 GHz
IF BW	10 Hz
Sweep points	4096
CW frequency	10 GHz
Time resolution	0.25 ns
Transmitted power	−10 dBm
Dynamic range	110 dB
Noise floor	−120 dBm
Patch antennas characteristics	Gain: 7.7 dBi; frequency 10.525 GHz
Horn antennas characteristics	Gain: 13.8 dBi; frequency 10.50 GHz
A pair of 5 m Teledyne storm microwave flexible Coaxial cables	9.4723 dB
Power amplifier (PA: PE15A4006)	30 dB Gain
Low noise amplifier (LNA: PE15A1026)	30 dB Gain

From the results of Figure 5, it can be concluded that the patch antennas generate more fluctuations on the received power. This is due to their half power beam-width of 87.14° in the E plane, resulting in an increased multipath contribution adding at times constructively and other times destructively. In Figures 5(a) and 5(c), it is observed that the multipath causes extensive fluctuation in the received signal, producing deep fades at particular locations. Concerning the horn antennas setup results, presented in Figures 5(b) and 5(d), the small scale fading is less important than those occurring with patch antennas setup. This is due to the fact that the horn antennas are characterized by a narrow half power beam-width of 30° . Hence, these antennas favor the LOS and the multipath signals traveling the

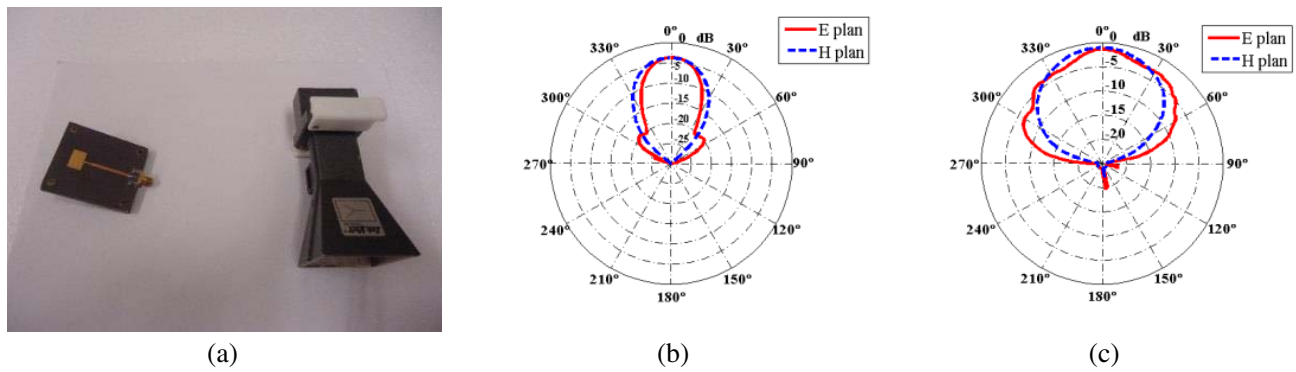


Figure 4. (a) Antennas models used, (b) horn antennas radiation pattern, (c) patch antenna radiation pattern.

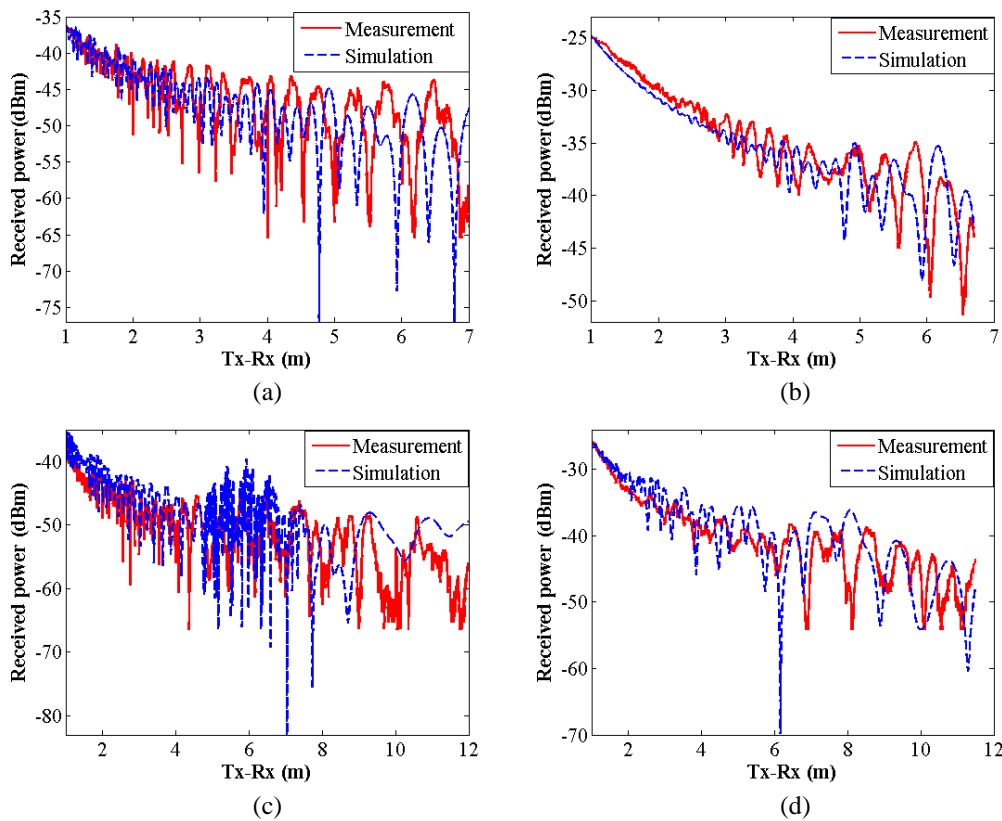


Figure 5. Received power in terms of antennas separation distance (Tx-Rx). (a) Patch-patch (smooth). (b) Horn-horn (smooth). (c) Patch-patch (rough). (d) Horn-horn (rough).

smallest distances (losing a minimum power along the way). Moreover, since the detectable number of multipath signals for the horn antennas setup is smaller than that of the patch antennas setup, the destructive power combining is less likely to occur. As can be observed from Figures 5(a) and 5(c), which correspond to the smooth and rough corridor, respectively, when the pair of antennas used is patch-patch, the roughness effect due to the semi-cylinders is perceptible. For the Tx-Rx separations lower than 4 meters, the roughness effect is less obvious. It becomes clearly noticeable around 4.7 m and beyond. This roughness effect increases the average power at the receiver, which results in a less steeply decayed curves corresponding to the rough tunnel. The same behavior is observed when the patch-patch antennas are replaced by horn-horn antennas. This scenario is illustrated in Figures 5(b) and 5(d) for the smooth and rough corridors, respectively. Furthermore, in both antenna setups, measurement results are in excellent agreement with those of the proposed model. Few differences are observed in the deep fades due to the fact that the model is limited in terms of multipath combinations.

4.2. Wideband Results

The wideband channel parameters are essential for the characterization of radio channels. They are used to quantify the time dispersion and frequency-selectivity of the channel. This study uses the frequency response analysis in order to derive and analyse the PDP of the channel. Using the PDP, the characteristics of the multipath fading channel is specified. In order to obtain the PDP, two different approaches have been used. First, wideband measurements have been carried out using the VNA as described in Section 3. The VNA sweeps the channel at discrete frequencies $f_k = f_0 + k\Delta f$ with $0 \leq k < 4096$, where $\Delta f = 976.6$ kHz is the frequency resolution within the frequency band or bandwidth parameter (B). This means that 4096 samples of the frequency response's magnitudes and phases are collected, in B from 8 GHz to 12 GHz. During measurements, the transmitter is fixed while the receiver

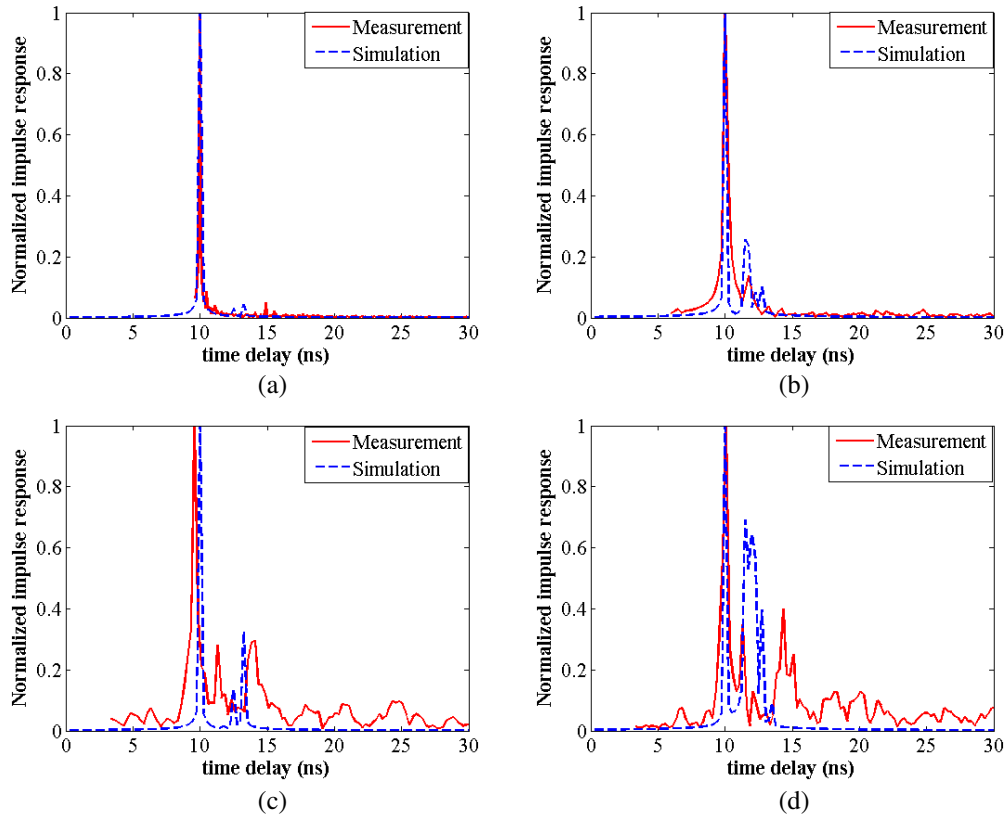


Figure 6. Channel impulse responses for Tx-Rx separation distance of 3 m. (a) Horn-horn (smooth). (b) Horn-horn (rough). (c) Patch-patch (smooth). (d) Patch-patch (rough).

is moved to 30 different locations. At each of the 30 locations, measurements are collected in 3 samples and then averaged. The complex frequency response at each location is normalized by the response at the reference position (when Tx and Rx are separated by 1m at LOS) [26, 29, 30].

The next step consists in using the Inverse Fourier transform (IFT) in order to get the channel impulse response as illustrated in Figure 6.

The PDP is then obtained as the square of the impulse response. Moreover, in order to validate the wideband model (described by (6), (7) and (8)), the impulse response of the corresponding frequency transfer function has been calculated using IFT. The resulting curve is compared with the corresponding measurement results. The impulse responses shown in Figure 6 demonstrate the dominance of the direct path over the other contributions for each case. This is due to the fact that the antennas are in LOS propagation condition from each other. For the horn-horn antennas scenario, there is a stronger dominance of the direct path than the secondary paths. This is a result of its greater directivity compared to patch antennas. However, it is noted that the roughness has the effect of increasing the number of secondary paths and also their contribution to the received energy. This can be observed by comparing Figures 6(a) and 6(b) for the pair of horn antennas and the Figures 6(c) and 6(d) for the pair of patch antennas. A peak detection algorithm is applied in order to determine the arrival times of the multipath signals. This allows describing the channel impulse response as a tap delay vector. In order to achieve path detection, a threshold level of -30 dB was considered. This eliminates the noise and improves the system performance. A detailed explanation regarding the peaks detection is represented in [31]. The considered multipath resolution for the PDP curves is $\Delta\tau = \frac{1}{B} = 0.25$ ns. Hence, the system can distinguish the signals with difference in path length greater than $\Delta d = c\Delta\tau = 7.5$ cm. Where $c = 3 \times 10^8$ m/s is the speed of light in vacuum. This condition is in agreement with the measurement approach used to carry out the experiment.

Using the tap delay profile in Figure 6, the RMS delay spread and the K factor curves have been

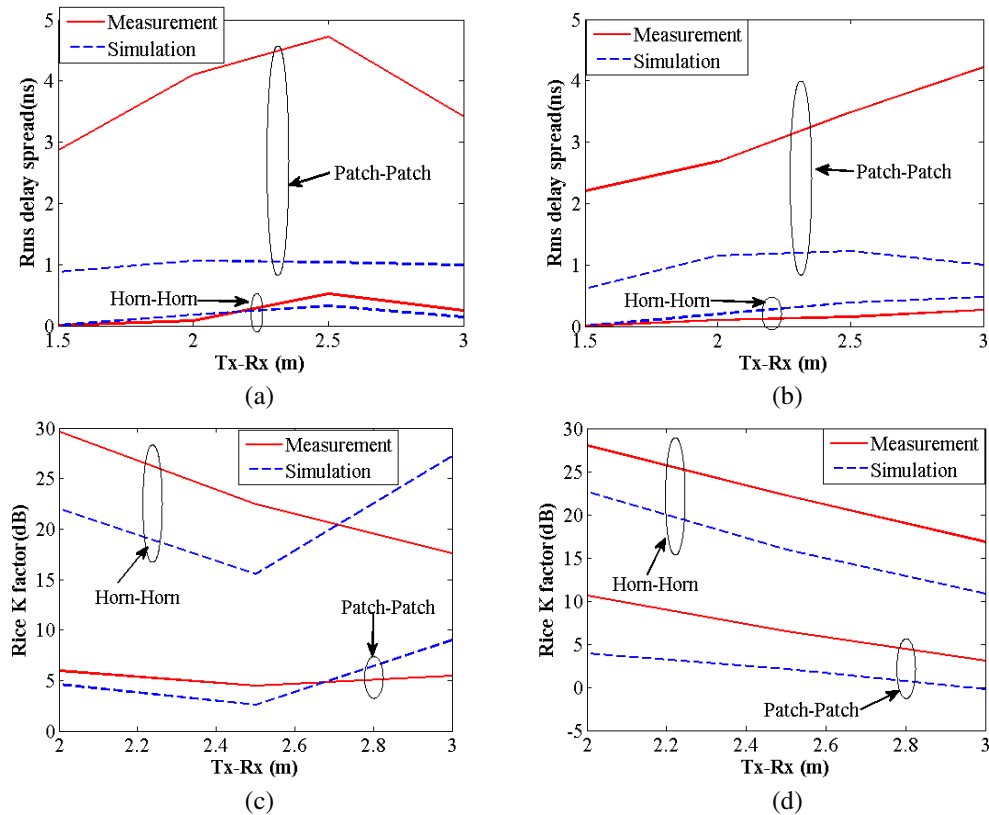


Figure 7. Rms delay spread and K factor in terms of Tx-Rx separation distance. (a) RMS delay spread (smooth). (b) RMS delay spread (rough). (c) Rice K factor (smooth). (d) Rice K factor (rough).

derived. The comparison of the RMS delay spread and the K factor, based on the developed model and the measurements, is shown in Figure 7. Regarding the horn antenna setup, both the theoretical and experimental curves of the K factor and the RMS delay spread have the same behaviour and are in good agreement. As for the patch antennas, there is a difference between the measurement and model parameter values. This can be explained by the approximation made when modeling antenna patterns and the electrical properties of material. Moreover, it can be explained by the assumed maximum reflections and scattering (on the curved surface), which makes the number of detectable multipath signals substantially less than the realistic number of rays detected by the patch antennas (having a relatively large beam width). It can also be noted that the experimental RMS delay spread generally increases with distance due to the increase in the number of multipath detections. As expected, the K factor results express the opposite trend of those of the RMS delay spread. The K factor curves, based on measurements, generally decrease with the increase in distance. This is due to the fact that the K factor, which represents the relative strength of the direct and scattered components of the received signal, is inversely proportional to the sum of the multipath powers. However, as illustrated in Figures 7(c) and 7(d), the roughness tends to reduce K factor value in several receiver locations when the separation distance between antennas increases. This is partly due to the additional amount of multipath components generated by the roughness effect. The RMS delay spread increases as the antennas separation distance increases, for both antennas setup regarding rough corridor study, as seen in Figures 7(a) and 7(b). Furthermore, the roughness tends to reduce the delay spread at almost all Tx-Rx positions. However, a decrease of delay spread at the position of 3 m is observed for experimental results when corridor is smooth. This can be explained by the effect of corridor materials' electrical properties on the multipath components when the receiving antenna is moving.

4.3. Model Validation by Statistical Analysis of Results

A statistical analysis of the received power has been carried out with the purpose to validate the proposed model in Section 3. In order to get the large scale fading, the overall measured received power in Figure 5 has been filtered using a sliding window of 40λ wide, as illustrated in Figure 8 [32, 33].

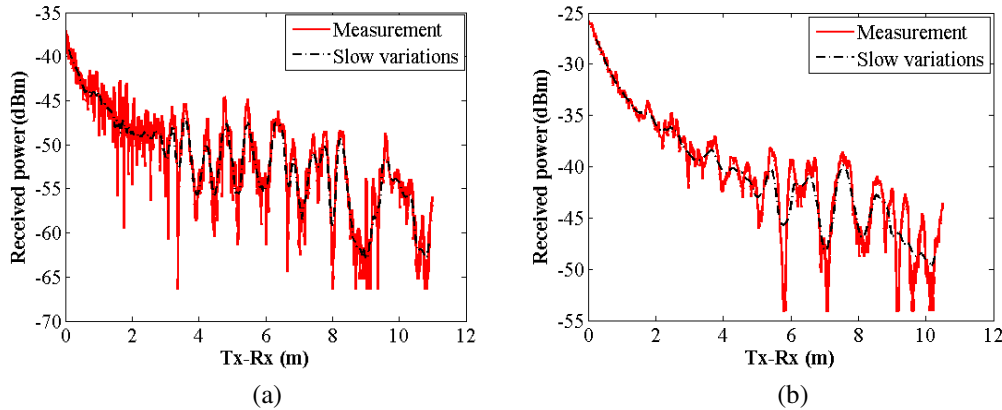


Figure 8. Small scale variations extraction by sliding window filtering. (a) Patch-patch (rough). (b) Horn-horn (rough).

Furthermore, a linear regression analysis (in log-log scale) is applied to these slowly varying curves, resulting in a straight line with a slope of n . This slope corresponds to the path loss exponent. Table 3 summarizes the statistical parameters of the two sets of antennas and specifies the standard deviation (Std) of minimum mean square error (MMSE) between the developed model and the measurements. The power prediction error is found to be less than 8 dB in all scenarios. Additionally, the path loss exponent follows the trend observed in most corridors and indoor areas when transmitter and receivers are located at the same floor in LOS configurations [34–37]. Its value for the patch antennas is less than 2. Hence, the propagation inside the corridor, when patch antennas are used, is not carried out under free space conditions. Instead, we observe a wave guiding effect.

Table 3. Statistics of measurement data for a rough corridor.

Type of antennas	Path loss exponent	Mean received power value (dBm)	Max received power value (dBm)	Std of received power value	Std of MMSE between measurement and model
Patch-Patch	1.6	-48.35	-34.39	5.735	7.19
Horn-Horn	2	-39.02	-24.93	3.731	5.84

Equation (9) is used to compute the Std of the MMSE [38]:

$$\sigma_{MMSE} = \sqrt{\frac{1}{N} \sum_{i=1}^N [PL_{measured}(d_i) - PL_{model}(d_i)]^2} \tag{9}$$

The cumulative distribution functions (CDFs) of the received powers, based on the proposed model and the measurements, are noted in Figure 9. It is observed that the measurements and the model’s results are in good agreement.

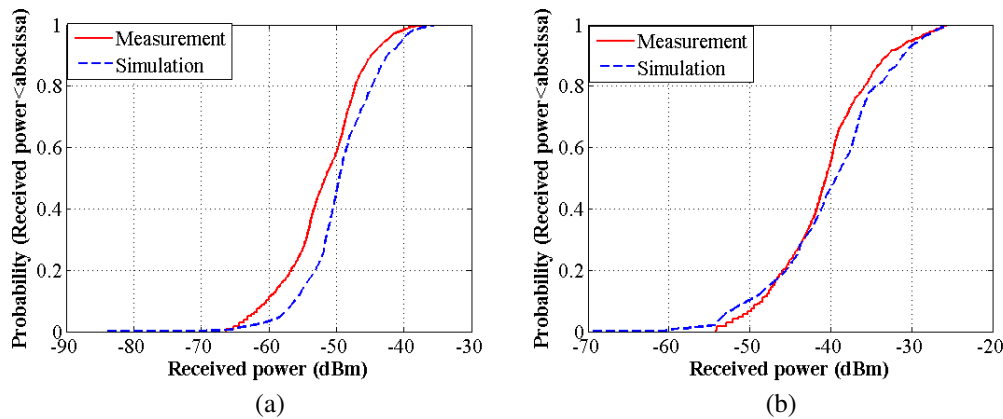


Figure 9. CDFs of the received powers based on the measurements and the proposed model (rough corridor). (a) Patch antennas case. (b) Horn antennas case.

5. CONCLUSION

An analytical model combining ray-tracing with UTD has been proposed. Narrowband and wideband parameters have been derived through simulations and compared to those of the experimental measurements. The deterministic model is able to predict radio wave propagation in a rough tunnel with periodical profile. The theoretical and experimental curves of the K factor and the RMS delay spread showed good agreement for the set of horn antennas. However, the set of patch antennas showed a small discrepancy between the theoretical and the measured RMS delay spread, due to the model limitation in terms of the number of reflected and scattered rays on rough profile. Important statistical parameters have been computed and analyzed for the complex confined area measurements. A wave guiding effect has been observed for the patch antenna measurements. Moreover, the power prediction error is found to be less than 8 dB. Despite the lack of information about electrical properties of the indoor materials, a good agreement has been observed between the proposed model and the measurement results. The proposed model of this work can be adapted to any environment having a periodic roughness. This work opens the door for studying structures with different periodic roughness, such as a pyramidal roughness.

ACKNOWLEDGMENT

The authors acknowledge with deep gratitude the financial support of the Natural Science and Engineering Research Council (NSERC) of Canada.

REFERENCES

1. Lim, S. Y., Z. Yun, and M. F. Iskander, "Propagation measurement and modeling for indoor stairwells at 2.4 and 5.8 GHz," *IEEE Transactions on Antennas and Propagation*, Vol. 62, 4754–4761, 2014.
2. Lim, S. Y., A. K. Awelemdy, Z. Yun, and M. F. Iskander, "Experimental study of propagation characteristics in an open-trench drain," *IEEE Antennas and Wireless Propagation Letters*, Vol. 15, 60–63, 2016.
3. Tarng, J. H., W. R. Chang, and B. J. Hsu, "Three-dimensional modeling of 900-MHz and 2.44-GHz radio propagation in corridors," *IEEE Transactions on Vehicular Technology*, Vol. 46, 519–527, 1997.
4. Brown, T., E. De Carvalho, and P. Kyritsi, "Index," *Practical Guide to the MIMO Radio Channel with MATLAB Examples*, 144–192, John Wiley & Sons, Ltd., Ed., 2012.
5. Hrovat, A., G. Kandus, and T. Javornik, "A survey of radio propagation modeling for tunnels," *IEEE Communications Surveys & Tutorials*, Vol. 16, 658–669, 2014.
6. Tarng, J. H., L. Wen-Shun, H. Yeh-Fong, and H. Jiunn-Ming, "A novel and efficient hybrid model of radio multipath-fading channels in indoor environments," *IEEE Transactions on Antennas and Propagation*, Vol. 51, 585–594, 2003.
7. Polivka, M., M. Svanda, P. Hudec, and S. Zvanovec, "UHF RF identification of people in indoor and open areas," *IEEE Transactions on Microwave Theory and Techniques*, Vol. 57, 1341–1347, 2009.
8. Geng, S. and P. Vainikainen, "Millimeter-wave propagation in indoor corridors," *IEEE Antennas and Wireless Propagation Letters*, Vol. 8, 1242–1245, 2009.
9. Helhel, S., "Comparison of 900 and 1800 MHz indoor propagation deterioration," *IEEE Transactions on Antennas and Propagation*, Vol. 54, 3921–3924, 2006.
10. Fono, V. A., L. Talbi, and N. Hakem, "Propagation modeling in complex rough environment based on ray tracing," *IEEE Antennas and Propagation Society International Symposium (APSURSI), 2013*, 1924–1925, 2013.
11. General Headquarters of Civil Defence, Ministry of Interior, United Arab Emirates, (2011, June 20, 2016), *UAE Fire and Life Safety Code of Practice*, Available: www.dcd.gov.ae/portal/eng/UAEFIRECODE_ENG.pdf.
12. Castel Fire, (June 20), *General Fire Suppression*, Available: <http://www.castlefire.co.uk/legacy/pages/suppression/gensupp.html>.
13. Fire Service Department of the Government of Hong Kong, (June 20, 2016), *Code of Practice for the Storage and Use of Special Gases in the Micro-electronics Industry*, Available: http://www.hkfsd.gov.hk/eng/source/licensing/storage_special_gas.pdf.
14. TOMCO2 Fire Systems. (June 20, 2016), *High Pressure CO2 Engineering, Installation and Operation Manual*, Available: www.tomcosystems.com/wp-content/uploads/2013/09/HPCO2_Engineering_Manual.pdf.
15. Yang, C.-F., B.-C. Wu, and C.-J. Ko, "A ray-tracing method for modeling indoor wave propagation and penetration," *IEEE Transactions on Antennas and Propagation*, Vol. 46, 907–919, 1998.
16. Sidhu, S. S., A. Khosla, and A. Sharma, "Implementation of 3-D Ray tracing propagation model for indoor wireless communication," *International Journal of Electronics Engineering*, Vol. 4, No. 1, 43–47, 2012.
17. International Telecommunications Union Radiocommunications, Sector (ITU-R), (2012, June 20, 2016), "Propagation data and prediction methods for the planning of indoor radiocommunications

- systems and radio local area networks in the frequency range 900 MHz to 100 GHz, Recommendation ITU-R P.1238-7 (02/2012),” Available: <https://www.itu.int/rec/R-REC-P.1238/fr>.
18. McNamara, D. A., C. W. I. Pistorius, and J. A. G. Malherbe, *Introduction to the Uniform Geometrical Theory of Diffraction*, Artech House, 1990.
 19. Pathak, P., W. Burnside, and R. Marhefka, “A uniform GTD analysis of the diffraction of electromagnetic waves by a smooth convex surface,” *IEEE Transactions on Antennas and Propagation*, Vol. 28, 631–642, 1980.
 20. Ghaddar, M., L. Talbi, G. Y. Delisle, and J. LeBel, “Deflecting-obstacle effects on signal propagation in the 60 GHz band,” *IEEE Transactions on Antennas and Propagation*, Vol. 61, 403–414, 2013.
 21. Han, C., A. O. Bicen, and I. F. Akyildiz, “Multi-ray channel modeling and wideband characterization for wireless communications in the terahertz band,” *IEEE Transactions on Wireless Communications*, Vol. 14, 2402–2412, 2015.
 22. El Azhari, M., M. Nedil, I. B. Mabrouk, K. Ghanem, and L. Talbi, “Characterization of an off-body channel at 2.45 GHz in an underground mine environment,” *Progress In Electromagnetics Research M*, Vol. 43, 91–100, 2015.
 23. Keysight Technologies, (June 20), *Keysight 2-port and 4-port PNA-X Network Analyzer, N5247A-10 MHz to 67 GHz*, Available: literature.cdn.keysight.com/litweb/pdf/N5247-90002.pdf.
 24. ST Electronics, (June 20), *MSAN-001 X-band Microwave Motion Sensor Module Application Note*, Available: www.limpkin.fr/public/HB100/HB100_Microwave_Sensor_Application_Note.pdf.
 25. Durgin, G. D. and T. S. Rappaport, “Theory of multipath shape factors for small-scale fading wireless channels,” *IEEE Transactions on Antennas and Propagation*, Vol. 48, 682–693, 2000.
 26. Kremono, H., “On the spatial and temporal coherence of wireless vehicular short range channels,” 2011.
 27. Gans, M. J., “A power-spectral theory of propagation in the mobile-radio environment,” *IEEE Transactions on Vehicular Technology*, Vol. 21, 27–38, 1972.
 28. Clarke, R. H., “A statistical theory of mobile-radio reception,” *Bell System Technical Journal*, Vol. 47, 957–1000, 1968.
 29. Keysight Technologies, (June 20), “Applying error correction to network analyzer measurements,” Available: literature.cdn.keysight.com/litweb/pdf/5965-7709E.pdf.
 30. Varela, M. S. and M. G. Sanchez, “RMS delay and coherence bandwidth measurements in indoor radio channels in the UHF band,” *IEEE Transactions on Vehicular Technology*, Vol. 50, 515–525, 2001.
 31. Pahlavan, K. and A. H. Levesque, “Measurement of wideband and UWB channel characteristics,” *Wireless Information Networks*, 149–203, John Wiley & Sons, Inc., Ed., 2005.
 32. Wang, Q., B. Ai, K. Guan, D. W. Matolak, R. He, and X. Zhou, “Ray-based statistical propagation modeling for indoor corridor scenarios at 15 GHz,” *International Journal of Antennas and Propagation*, Vol. 2016, 12, 2016.
 33. Valenzuela, R. A., O. Landron, and D. L. Jacobs, “Estimating local mean signal strength of indoor multipath propagation,” *IEEE Transactions on Vehicular Technology*, Vol. 46, 203–212, 1997.
 34. Rappaport, T. S., *Wireless Communications: Principles and Practice*, Prentice Hall PTR, 2002.
 35. Deng, S., M. K. Samimi, and T. S. Rappaport, “28 GHz and 73 GHz millimeter-wave indoor propagation measurements and path loss models,” *2015 IEEE International Conference on Communication Workshop (ICCW)*, 1244–1250, 2015.
 36. Chan, K. M., A. Subic, F. Fuss, P. Clifton, J. A. Kirkup, D. D. Rowlands, et al., “6th Asia-Pacific congress on sports technology (APCST) indoor propagation investigation from a 2.4 GHz waist mounted beacon,” *Procedia Engineering*, Vol. 60, 188–194, Jan. 1, 2013.
 37. Maccartney, G. R., T. S. Rappaport, S. Sun, and S. Deng, “Indoor office wideband millimeter-wave propagation measurements and channel models at 28 and 73 GHz for ultra-dense 5G wireless networks,” *IEEE Access*, Vol. 3, 2388–2424, 2015.
 38. Goldsmith, A., *Wireless Communications*, Cambridge University Press, 2005.